Supplementary information: Light-driven extremely nonlinear bulk photogalvanic currents

Ofer Neufeld[1,*], Nicolas Tancogne-Dejean[1], Umberto De Giovannini[1,2,3], Hannes Hübener[1], Angel Rubio[1,3,4]

[1]Max Planck Institute for the Structure and Dynamics of Matter, Hamburg, Germany, 22761.
[2]IKERBASQUE, Basque Foundation for Science, E-48011, Bilbao, Spain.
[3]Nano-Bio Spectroscopy Group, Universidad del País Vasco UPV/EHU-20018 San Sebastián, Spain.
[4]Center for Computational Quantum Physics (CCQ), The Flatiron Institute, New York, NY, USA, 10010.

*Corresponding authors E-mail: ofer.neufeld@gmail.com, angel.rubio@mpsd.mpg.de

COMPUTATIONAL DETAILS

We report here on technical details for the calculations presented in the main text. We start by presenting the methodological approach utilized in the main text that is based on time-dependent density functional theory (TDDFT). All DFT calculations were performed using the real-space grid-based code, octopus [1–3]. The Kohn Sham (KS) equations were discretized on a Cartesian grid with the shape of the primitive lattice cell in each material system, where atomic geometries and lattice parameters were taken at the experimental values. Calculations were performed using the local density approximation (LDA), and in some cases also using the Perdew–Burke–Ernzerhof (PBE) exchange-correlation (XC) functional [4]. Spin degrees of freedom and spin-orbit couplings were neglected. The frozen core approximation was used for inner core bands which were treated with norm-conserving pseudopotentials [5]. The KS equations were solved to self-consistency with a tolerance $<10^{-7}$ Hartree, and the grid spacing was converged in each material system to $\Delta x = \Delta y = \Delta z = 0.33$ Bohr in diamond, 0.35 Bohr in Si, 0.3 bohr in MgO, 0.4 Bohr in monolayer hBN, and 0.4 Bohr in graphene. We employed a Γ-centered k-grid in each system, which converged the time-dependent current expectation value: $36\times36\times36$ k-grid in diamond, $24\times24\times24$ k-grid in Si, $32\times32\times32$ k-grid in MgO, $36\times36\times1$ k-grid in monolayer hBN, and $120\times120\times1$ k-grid in graphene.

For TDDFT calculations, we solved the time-dependent KS equations within the adiabatic approximation, represented in real-space and in the velocity gauge, given in atomic units by:

$$i\partial_t \left|\varphi_{n,k}^{KS}(t)\right\rangle = \left(\frac{1}{2}\left(-i\nabla + \frac{\mathbf{A}(t)}{c}\right)^2 + v_{KS}(\mathbf{r},t) \right)\left|\varphi_{n,k}^{KS}(t)\right\rangle \tag{1}$$

where $\left|\varphi_{n,k}^{KS}(t)\right\rangle$ is the KS-Bloch state at k-point k and band n, $\mathbf{A}(t)$ is the vector potential of the laser electric field within the dipole approximation, such that $-\partial_t \mathbf{A}(t) = c\mathbf{E}(t)$, c is the speed of light in atomic units ($c\approx137.036$), and $v_{KS}(\mathbf{r},t)$ is the time-dependent KS potential given by:

$$v_{KS}(\mathbf{r},t) = -\sum_I \frac{Z_I}{|\mathbf{R}_I - \mathbf{r}|} + \int d^3r' \frac{n(\mathbf{r}',t)}{|\mathbf{r}-\mathbf{r}'|} + v_{XC}[n(\mathbf{r},t)] \tag{2}$$

where Z_I is the charge of the I'th nuclei and $\mathbf{R}_I$ is its coordinate, v_{XC} is the XC potential that is a functional of $n(\mathbf{r},t) = \sum_{n,k}\left|\left|\varphi_{n,k}^{KS}(t)\right\rangle\right|^2$, the time-dependent electron density. The KS wave functions were propagated with a time step of $\Delta t = 0.2$ a.u. which converged the time-dependent current in all material systems within the LDA. For TD-PBE calculations a time step of 0.08 a.u. was used. The initial state was taken to be the system's ground state. The propagator was represented by a Lanczos expansion.

For the independent particle approximation (IPA) calculations, the same methodology was utilized but where the KS potential was kept frozen to its initial form such that $v_{KS}[n(\mathbf{r},t)] \equiv v_{KS}[n(\mathbf{r},t=0)]$.

For the two-dimensional systems of monolayer hBN and graphene, we added additional vacuum spacing above and below the monolayer of 40 Bohr in each direction of the non-periodic axis, and absorbing boundaries were employed along this axis with a width of 12 Bohr.

The time-dependent current expectation value was calculated directly from the time-dependent KS states as:

$$\mathbf{J}(t) = \frac{1}{\Omega} \int_{\Omega} d^3r \, \mathbf{j}(\mathbf{r}, t) \tag{3}$$

where $\mathbf{j}(\mathbf{r}, t)$ is the microscopic time-dependent current density:

$$\mathbf{j}(\mathbf{r}, t) = \frac{1}{2} \sum_{n,k} \left[\varphi_{n,k}^{KS\,*}(r, t) \left(-i\boldsymbol{\nabla} + \frac{\mathbf{A}(t)}{c} \right) \varphi_{n,k}^{KS}(r, t) + c.c. \right] \tag{4}$$

, and Ω represents the volume integral over the primitive cell (for 2D materials the volume is calculated with a width of 4 Bohr along the axis transverse to the monolayer). The photocurrent was calculated as $\mathbf{I} = \mathbf{J}(t \to \infty)$ when the laser pulse has ended for 3D systems, and averaged over one laser cycle after the pulse ends for 2D systems (to remove oscillations due to superposition states). Note that within real-time KS-TDDFT the time-dependent KS states remain fully occupied and are comprised of a superposition of the field-free eigenstates of the system. For results presented in the SI, the harmonic spectrum was calculated as the Fourier transform of the first derivative of the current:

$$I(\omega) = \left| \int dt \, \partial_t \mathbf{J}(t) e^{-i\omega t} \right|^2 \tag{5}$$

, which was evaluated numerically with an 8'th order finite-difference approximation for the temporal derivative, and fast Fourier transforms.

Band and k-point occupations were computed by calculating the projections of the time-dependent KS states on the field-free states at $t=0$. For Figures 3(a,b) in the main text, the occupations were integrated in k-space and normalized to the density of states at each k-point, g(k).

The envelope function of the employed laser pulse, $f(t)$, was taken to be of the following 'super-sine' form [6]:

$$f(t) = \left(sin\left(\pi \frac{t}{T_p} \right) \right)^{\left(\frac{\left| \pi \left(\frac{t}{T_p} - \frac{1}{2} \right) \right|}{\sigma} \right)} \tag{6}$$

where σ=0.75, T_p is the duration of the laser pulse which was taken to be T_p=8T (unless stated otherwise), where T is a single cycle of the fundamental carrier frequency. This form is roughly analogous to a super-gaussian pulse, but where the field starts and ends exactly at 0 which is more convenient numerically.

ADDITIONAL RESULTS IN DIAMOND

We present here additional results complementary to those presented in the main text. First, we show that the photocurrents arise even when utilizing a PBE XC functional, and similarly to the TD-LDA calculations presented in the main text, they do not decay over the timescale of the simulation. Figure S1(a) shows the time-dependent current expectation value calculated in diamond with PBE XC. The current arises only along the y-axis transverse to the field's mirror plane and remains constant in time even long after the pulse has ended. This supports the conclusions in the main text that the excited current-carrying state is an eigenstate of the many-body system and will only decay *via* radiative or scattering channels that are not included in our simulation.

Next, Fig. S1(b) shows the calculated time-dependent current expectation value driven in a diamond lattice within the (110) planes (unlike figures in the main text that present currents driven in the (111) planes). The (110) planes have a local four-fold symmetry that is different than that in the (111) planes. Still, the current arises along the field's y-axis, demonstrating similar control over the current direction. This supports the conclusion that the current generation mechanism is largely unaffected by the local lattice structure and symmetry.
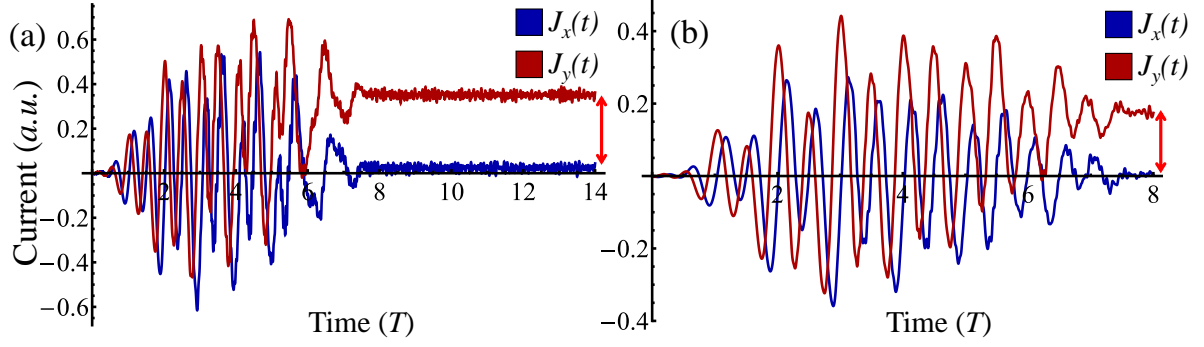
FIG. S1. Additional calculations of photocurrents in diamond. (a) Time-dependent current expectation value calculated using PBE XC, showing results similar to those obtained within the LDA (for laser parameters $\lambda=1200$nm, $\Delta=\sqrt{3}$, $I_0=7.5\times10^{12}$ W/cm^2). (b) Time-dependent current expectation value calculated where $\mathbf{E}(t)$ is polarized in the diamond (110) planes, showing that that the photocurrent is still directed along the field's y-axis regardless of the different local symmetry compared to the (111) planes (calculated for similar laser parameters as in (a), except that $\Delta=1$). Arrows indicate the residual photocurrent. The current is given in 10^{-3} atomic units.

We next show that these currents are CEP-independent, just as one would expect for long-duration pulses. Fig. S2 shows calculated photocurrent amplitudes in diamond *vs.* the CEP for the same pulse durations as presented in the main text in Fig. 4(c). The resulting photocurrents are CEP-independent. This result further highlights that different physical effects come into play in higher laser powers, as discussed in the main text.
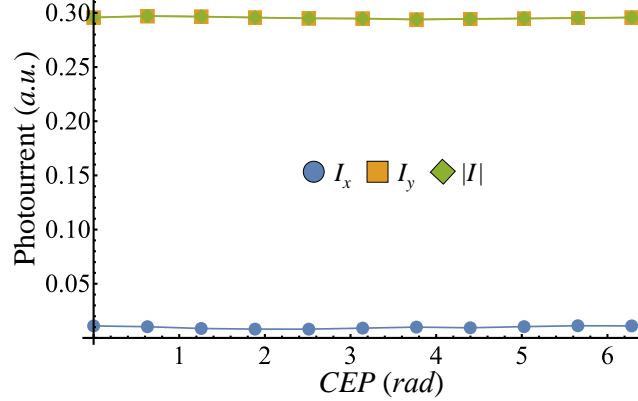

FIG. S2. CEP-independence of photocurrents in diamond for laser powers smaller than 10^{13} W/cm^2. Driven photocurrent amplitudes in diamond (111) planes *vs.* the CEP (calculated for $\lambda=1200$nm, $\Delta=\sqrt{2}$, $I_0=7.5\times10^{12}$ W/cm^2 and 8-cycle long laser pulses). The current is given in 10^{-3} atomic units.

Lastly, we explore deviations from the IPA for strongly-driven diamond in the regime of laser powers above 10^{13} W/cm^2. Results in the main text (Fig. 4(b)) showed that there are considerable deviations in the obtained photocurrents upon inclusion/exclusion of dynamical electron-electron interactions (up to 20%), as well as an onset of x-polarized photocurrents. We show here that in these conditions similar effects arise in the HHG emission. In this case deviations are even larger and can reach values of 100% for some harmonics, indicating the breakdown of the IPA. Figure S3(a) presents the calculated HHG spectra in this regime from the co-circular ω-2ω field for $I_0=5\times10^{13}$ W/cm^2, showing these extreme deviations. Figure S3(b) shows that when averaged over the first 60 harmonic orders, these deviations increase in correspondence with the laser power, similar to the photocurrent deviations. Overall, this further validates the onset of strong laser-induced many-body effects in this intense regime.
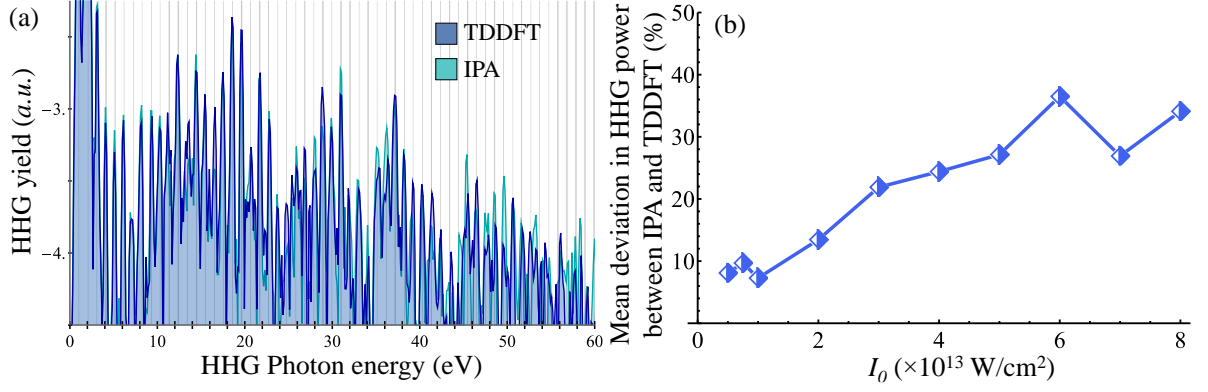
FIG. S3. Breakdown of the IPA in strongly-driven diamond in the HHG spectrum. (a) Calculated HHG spectra (log scale) within the IPA and full TDDFT calculation for $\lambda=1200nm$, $\Delta=\sqrt{3}$, $I_0=5\times10^{13}$ W/cm^2. Gray lines indicate positions of integer harmonic orders for this wavelength. The plot shows that considerable deviations arise in the HHG power in this regime due to dynamical correlations. (b) Average deviation in harmonic power between the full TDDFT calculation and the IPA *vs.* the laser power (averaged over first 60 harmonics).

ADDITIONAL RESULTS IN OTHER SYSTEMS

We present additional results of photocurrent excitation in other material systems. We start by exploring several three-dimensional bulk solids. Figure S4 presents calculated time-dependent photocurrents in Si (in the (111) planes), and MgO (in the (111) planes), after interaction with intense co-circular ω-2ω pulses. These results are analogous to those presented in the main text for diamond and highlight that the photocurrent and its generation mechanism is largely independent of the material system and its chemical and physical properties. In particular, the current is always observed transverse to the field's mirror axis, and is generated even though the laser pulses are of long duration and have photon energies much smaller than the band gap in each case.
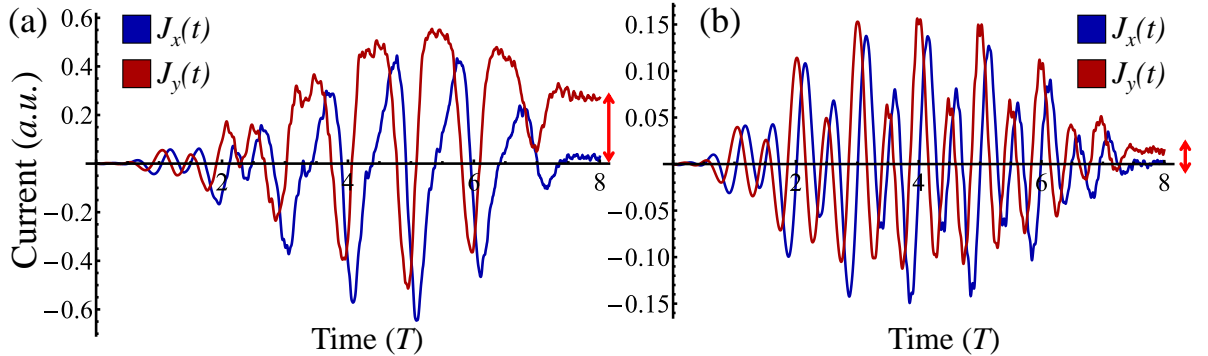

FIG. S4. Calculations of photocurrents in Si and MgO. (a) Time-dependent current expectation value in Si (for laser parameters $\lambda=2500nm$, $\Delta=1$, $I_0=10^{12}$ W/cm^2). (b) Time-dependent current expectation value in MgO (for laser parameters $\lambda=1200nm$, $\Delta=1$, $I_0=5\times10^{12}$ W/cm^2). Arrows indicate the residual photocurrent. The current is given in 10^{-3} atomic units.

We next investigate photocurrents in two-dimensional systems. Figure S5 presents investigation of photocurrent generation in monolayer hBN where the field is polarized within the monolayer (*xy* plane). Figure S5(a) shows that similar photocurrents arise, and that they are transverse to the field's mirror axis. We note that this occurs even though hBN monolayers lack inversion symmetry. Figure S5(b) shows the *k*-space occupations of the CB after the laser pulse has ended, clearly indicating that there is no *k*-inversion symmetry (i.e. a residual current is generated). Notably, in this case no symmetries remain in the *k*-space occupations, but the current is still mainly polarized along the *y*-axis, indicating that its directionality is largely determined by the field's properties rather than those of the material system. We also note that, as expected, the occupations of the K and K' valleys are now asymmetric, allowing for a mechanism to generate valley polarization. This is in accordance with similar results presented with counter-rotating bi-circular fields [7].
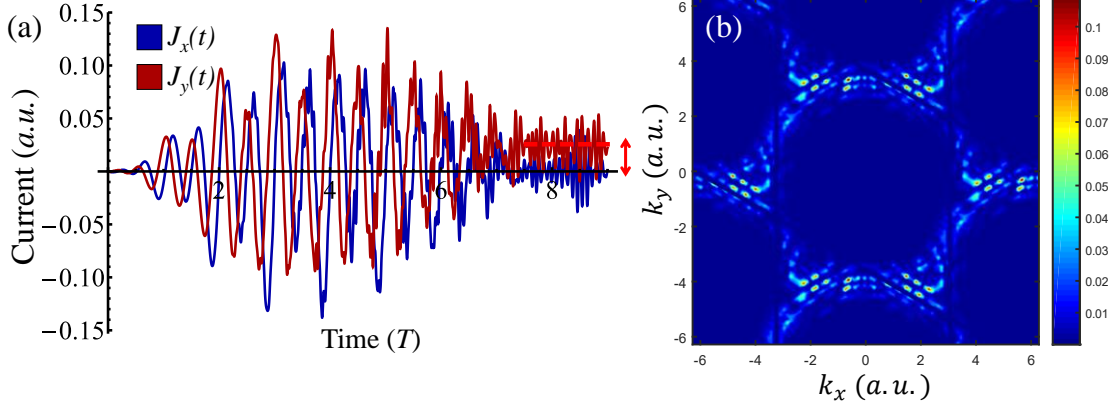
FIG. S5. Photocurrent generation in monolayer hBN. (a) Time-dependent current expectation value calculated for λ=2500nm, Δ=√2, $I_0=10^{12}$ W/cm^2). Arrow and dashed line indicate the residual photocurrent. (b) CB occupations in k-space after the pulse has ended showing an asymmetric occupation pattern around the K and K' points. The current is given in 10^{-3} atomic units.

We move on to graphene, which is a hexagonal Dirac semi-metal with band touching at the K and K' points. Previous theoretical and experimental work showed that one can generate strongly-driven photocurrents in graphene with monochromatic few-cycle laser pulses [8–11]. Figure S6 explores current injection from the co-rotating ω-2ω field, showing that similar effects occur in the long-pulse regime (the field is polarized within the graphene sheet). This effect is seen both for shorter wavelengths (1200-600nm, see Fig. S6(a,b)), and for much longer wavelengths in the THz regime (2500-1250nm, see Fig. S6(c,d)). We note that for all tested wavelengths the k-space occupations exhibit an exact mirror symmetry, in accordance with the formal analysis presented in the main text (and because graphene is inversion-symmetric). Thus, the total populations of the K and K' valleys are identical and connected through a mirror symmetry, which is mediated by the generalized time-reversal symmetry of the ω-2ω co-rotating field. Nonetheless, photocurrents arise because the occupation patterns are extremely asymmetric between the K and K' valleys (this is also evident locally in the region near each K and the K' band touching point).
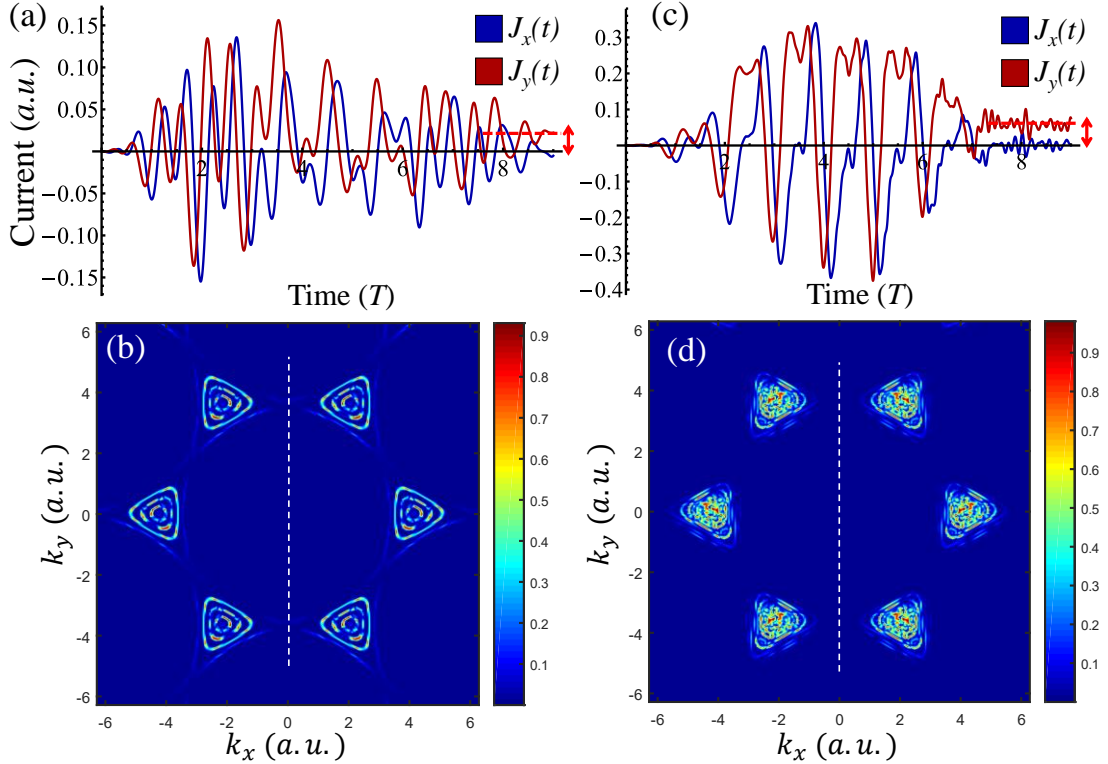

FIG. S6. Photocurrent generation in graphene. (a) Time-dependent current expectation value calculated for λ=1200nm, Δ=√2, $I_0=10^{11}$ W/cm^2. (b) CB occupations in k-space after the pulse has ended corresponding to the parameters in (a). (c,d) Same as in (a,b), but for λ=2500nm. Arrows and dashed lines indicate the residual photocurrents. White dashed lines mark a mirror symmetry for k-space occupations that connects the K and K' points, and forbids x-polarized photocurrents. The current is given in 10^{-3} atomic units.

SUPPLEMENTARY REFERENCES

[1]   A. Castro, H. Appel, M. Oliveira, C. A. Rozzi, X. Andrade, F. Lorenzen, M. A. L. Marques, E. K. U. Gross, and A. Rubio, *Octopus: A Tool for the Application of Time-Dependent Density Functional Theory*, Phys. Status Solidi **243**, 2465 (2006).

[2]   X. Andrade, D. Strubbe, U. De Giovannini, H. Larsen, M. J. T. Oliveira, J. Alberdi-rodriguez, A. Varas, I. Theophilou, N. Helbig, M. J. Verstraete, L. Stella, F. Nogueira, A. Castro, M. A. L. Marques, and A. Rubio, *Real-Space Grids and the Octopus Code as Tools for the Development of New Simulation Approaches for Electronic Systems*, Phys. Chem. Chem. Phys. **17**, 31371 (2015).

[3]   N. Tancogne-Dejean, M. J. T. Oliveira, X. Andrade, H. Appel, C. H. Borca, G. Le Breton, F. Buchholz, A. Castro, S. Corni, A. A. Correa, U. De Giovannini, A. Delgado, F. G. Eich, J. Flick, G. Gil, A. Gomez, N. Helbig, H. Hübener, R. Jestädt, J. Jornet-Somoza, A. H. Larsen, I. V Lebedeva, M. Lüders, M. A. L. Marques, S. T. Ohlmann, S. Pipolo, M. Rampp, C. A. Rozzi, D. A. Strubbe, S. A. Sato, C. Schäfer, I. Theophilou, A. Welden, and A. Rubio, *Octopus, a Computational Framework for Exploring Light-Driven Phenomena and Quantum Dynamics in Extended and Finite Systems*, J. Chem. Phys. **152**, 124119 (2020).

[4]   J. P. Perdew, K. Burke, and M. Ernzerhof, *Generalized Gradient Approximation Made Simple*, Phys. Rev. Lett. **77**, 3865 (1996).

[5]   C. Hartwigsen, S. Goedecker, and J. Hutter, *Relativistic Separable Dual-Space Gaussian Pseudopotentials from H to Rn*, Phys. Rev. B **58**, 3641 (1998).

[6]   O. Neufeld and O. Cohen, *Background-Free Measurement of Ring Currents by Symmetry-Breaking High-Harmonic Spectroscopy*, Phys. Rev. Lett. **123**, 103202 (2019).

[7]   Á. Jiménez-Galán, R. E. F. Silva, O. Smirnova, and M. Ivanov, *Lightwave Control of Topological Properties in 2D Materials for Sub-Cycle and Non-Resonant Valley Manipulation*, Nat. Photonics **14**, 728 (2020).

[8]   T. Higuchi, C. Heide, K. Ullmann, H. B. Weber, and P. Hommelhoff, *Light-Field-Driven Currents in Graphene*, Nature **550**, 224 (2017).

[9]   C. Heide, T. Higuchi, H. B. Weber, and P. Hommelhoff, *Coherent Electron Trajectory Control in Graphene*, Phys. Rev. Lett. **121**, 207401 (2018).

[10]   C. Heide, T. Boolakee, T. Higuchi, H. B. Weber, and P. Hommelhoff, *Interaction of Carrier Envelope Phase-Stable Laser Pulses with Graphene: The Transition from the Weak-Field to the Strong-Field Regime*, New J. Phys. **21**, 45003 (2019).

[11]   C. Heide, T. Boolakee, T. Higuchi, and P. Hommelhoff, *Sub-Cycle Temporal Evolution of Light-Induced Electron Dynamics in Hexagonal 2D Materials*, J. Phys. Photonics **2**, 24004 (2020).